PHYSICAL REVIEW E **94**, 042406 (2016)

Emergence of flagellar beating from the collective behavior of individual ATP-powered dyneins

S. Namdeo and P. R. Onck[*]

Zernike Institute for Advanced Materials, University of Groningen, 9747 AG Groningen, The Netherlands

(Received 21 January 2016; revised manuscript received 28 May 2016; published 10 October 2016)

Flagella are hair-like projections from the surface of eukaryotic cells, and they play an important role in many cellular functions, such as cell-motility. The beating of flagella is enabled by their internal architecture, the axoneme, and is powered by a dense distribution of motor proteins, dyneins. The dyneins deliver the required mechanical work through the hydrolysis of ATP. Although the dynein-ATP cycle, the axoneme microstructure, and the flagellar-beating kinematics are well studied, their integration into a coherent picture of ATP-powered flagellar beating is still lacking. Here we show that a time-delayed negative-work-based switching mechanism is able to convert the individual sliding action of hundreds of dyneins into a regular overall beating pattern leading to propulsion. We developed a computational model based on a minimal representation of the axoneme consisting of two representative doublet microtubules connected by nexin links. The relative sliding of the microtubules is incorporated by modeling two groups of ATP-powered dyneins, each responsible for sliding in opposite directions. A time-delayed switching mechanism is postulated, which is key in converting the local individual sliding action of multiple dyneins into global beating. Our results demonstrate that an overall nonreciprocal beating pattern can emerge with time due to the spatial and temporal coordination of the individual dyneins. These findings provide insights in the fundamental working mechanism of axonemal dyneins and could possibly open new research directions in the field of flagellar motility.

DOI: 10.1103/PhysRevE.94.042406

I. INTRODUCTION

Motor proteins are powered by the hydrolysis of ATP (adenosine triphosphate) molecules and convert chemical energy into mechanical work, responsible for many cellular functions. For instance, axonemal dyneins [Fig. 1(a)]—found in flagella and cilia—are crucial for cell motility and fluid transport (e.g., propulsion of spermatozoa and transport of mucus in trachea, respectively). Cilia and flagella are motile hair-like projections from the surface of (eukaryotic) cells, and have an identical microstructure called the axoneme [1]; see Fig. 1(b).[1] The axoneme consists of an array of nine doublet microtubules surrounding a pair of single microtubules (often referred to as the $9 \times 2 + 2$ configuration).[2] Each of the outer doublets is linked to its neighbors by protein filaments, called nexin links. The microtubules are filamentous proteins of α- and β-tubulin dimers that contain the binding sites for the dyneins [3–6]. The dyneins are anchored at one doublet microtubule ["A" in Figs. 1(a) and 1(b)] and interact with the neighboring microtubule ["B" in Figs. 1(a) and 1(b)]. It is commonly accepted that the force-transduction of the axonemal dyneins and their coordinated operation—along the length of the axoneme and in time—leads to repetitive episodes of bending (and bend propagation) responsible for the ciliary and flagellar waveforms [7–17]; e.g., see Fig. 1(c).

Axonemal dyneins generate force by coupling ATP hydrolysis to conformational changes, which causes sliding of the attached microtubules [3–7,21]; see Fig. 2. Each dynein comprises three basic units: a head, stalk, and stem; see Fig. 1(a). The head contains the ATP hydrolysis site, the stem anchors the dynein to the microtubule doublet, and the stalk contains (at its tip) an ATP-sensitive microtubule-binding domain [4]. The conformational change driven by ATP hydrolysis alters the angle between the stem and stalk, which causes (relative) sliding of the microtubules [4]. Binding of an ATP molecule causes a weak detachment of the stalk from the microtubule (denoted by [MT,Dyn] in Fig. 2), while hydrolysis of the ATP molecule leads to a rigor stalk-microtubule attachment ([MT.Dyn] in Fig. 2). The subsequent release of ADP and $\mathrm{P_i}$ is then responsible for a large conformational "power stroke" leading to the relative sliding of the microtubules [3–7,21,22]. The working cycle of a dynein can thus be interpreted as a cyclic execution of power and recovery strokes, see Fig. 2, making the dyneins periodic force generators [23], where the time period of the force generation is governed by the ATP hydrolysis cycle and depends on the concentration of ATP in the solution [23,24].

Although consensus has been reached on the three separate ingredients of flagellar beating (i.e., dynein cycle, axonemal microstructure, and flagellar kinematics), shown in Fig. 1, the integration of these ingredients into a coherent picture is still lacking. The challenge remains in understanding how the forces generated by thousands of individual dyneins at the nanoscale [Fig. 1(a)] can lead to smooth and regular beating at the micron scale [Fig. 1(c)], and how this is mediated by the structure of the axoneme [Fig. 1(b)]. The force-transduction of individual dynein molecules has been studied experimentally via optical-trap nanometry [23,25–28] and their collective behavior has been analyzed through microtubule-motility assays

---

[*] P.R.Onck@rug.nl

[1] Although cilia and flagella have an identical microstructure, they were given different names before their structures were studied. Typically, cells possess one or two long flagella, whereas ciliated cells have many short cilia. For example, the mammalian spermatozoon has a single flagellum, the unicellular green alga chlamydomonas has two flagella, and the unicellular protozoan paramecium is covered with a few thousand cilia, which are used both to move and to bring in food particles [2].

[2] Although variations in axoneme morphology are discovered, the structural aspects remain similar [1].

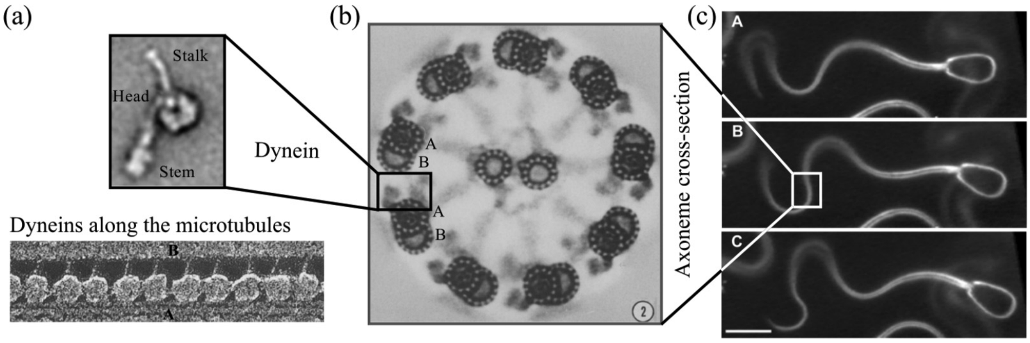

FIG. 1. (a) Structure of an axonemal dynein comprising three basic units: a head, stem, and stalk [3]. Presence of the dyneins (outer arms) at a regular spacing along the microtubules; see the lower panel [18]. (b) An electron micrograph of an axoneme cross-section showing the $9 \times 2 + 2$ configuration [19]. (c) Flagellar beating of a typical spermatozoon. The three video-fields (A-C) are 200 ms apart and the scale bar is 10 μm [20]. Figures are reproduced with permission of the copyright owner(s).

[25,29–34]. It has been generally accepted that the dyneins apply a sliding force during their working cycle leading to the generation of bending of the microtubules [8,10,35–37]. Large deflections can be generated by the accumulation of successive sliding events, while the microtubules remain of fixed length [1]. One aspect that has received considerable attention is the fact that the microstructure of the axoneme is inherently three-dimensional, while flagellar beating is planar. During a planar bend development not all the dynein motors found at a cross-section can generate active sliding at the same time [7,13], because axonemal dyneins are unidirectional motors, directed toward the minus-end of the microtubule polarity (basal end) [15]; see Fig. 3. The axoneme's geometry dictates that one group of dyneins is in an active state and produce sliding toward the basal end, while a second group of dyneins—positioned diametrically opposite to the first group—is in an inactive state (see Fig. 3). With time, the bending curvature at a specific location changes sign when the first group becomes inactive and the second group active (also known as the "switch-point" hypothesis) [8,15]. An important aspect that has remained elusive is the mechanism of coordination of the dyneins. How do thousands of individual dyneins coordinate their working cycle in order to produce traveling waves?

Observation of the flagellar kinematics (waveform and beating frequencies) indicates that there is a train of bends (of opposite curvature) along the axonemal length, which is traveling in time causing wave propagation and flagellar motility. The magnitude of the curvature can be linked to the amount of sliding displacement at a specific location relative to a reference value. Experimental observations point to the switching incidents during flagellar beating when the bending curvature changes sign caused by reversal of the sliding displacements [15]. Obviously, these switching points should move in a very controlled fashion along the length of the axoneme to cause wave propagation. These

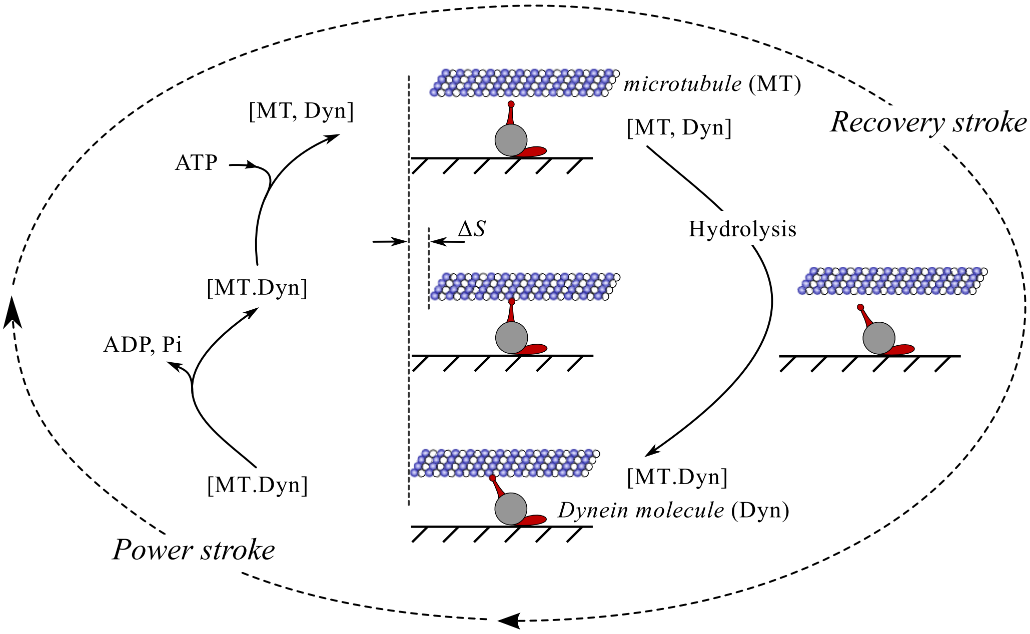

FIG. 2. ATP hydrolysis cycle, ATP $\rightleftharpoons$ ADP + P$_\mathrm{i}$, governing the power (and recovery) stroke of a dynein molecule leading to a conformational change and sliding of the attached microtubule.

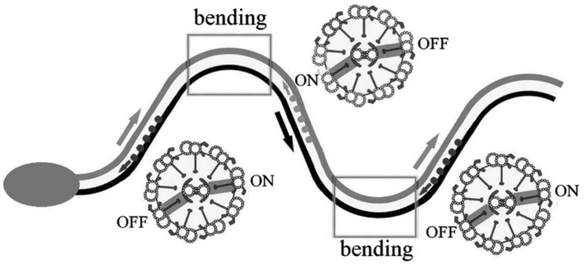

FIG. 3. During planar flagellar beating the dyneins are able to coordinate their operation along the axoneme length as well as at the three-dimensional axoneme cross-section. The unidirectional motion of the dyneins (denoted by the dots) are directed toward the basal end (minus end) of the microtubule, which is indicated by the small arrows. However, this action leads to sliding of the neighboring (attached) microtubule toward the distal end of the axoneme, which is indicated by the bigger arrows [13]. The figure is adopted from Ref. [13] and is reproduced with permission of the copyright owner.

observations have led to the "curvature control" hypothesis suggested by Brokaw [36,37], which implies that activation and deactivation of the dyneins are governed by a threshold curvature [8,9,15,38,39]. Computational studies based on the curvature control hypothesis—given preexisting curvatures along the axoneme length—predict steady oscillations and wave propagation only when there is a delay in the feedback loop from curvature to (de)-activation of the dyneins [8,9,15,35–37,39–41]. Another hypothesis was later suggested by Lindemann [42,43], known as the "geometric clutch" hypothesis in which the interdoublet spacing is linked to the binding probability (thus activation and deactivation) of the dyneins at a given cross-section of the axoneme. The geometric clutch hypothesis is closely related to the curvature control hypothesis since the development of curvature affects the interdoublet spacing [8]. Recently, a load-dependent response of the motor proteins was suggested to obtain flagellar beating in a mathematical study (also known as the "sliding control" hypothesis) [14]. In this work, it is hypothesized that elastic energy will accumulate due to the action of the dyneins, which causes deactivation of the dyneins once a threshold value is reached [8].

Clearly, many different hypotheses have been proposed in the literature, but no consensus has been reached so far. Existing theoretical models [8,9,14,15,35–37,39–43] are mostly based on geometry-controlled activation and deactivation of dynein forces, in which the inherent physical parameters of the dynein ATP-cycle are not accounted for. The goal of this article is therefore to take the independent ATP-driven force cycle of the dyneins as a starting point and explore how the overall beating pattern emerges from their collective behavior. We will explore how individual dyneins are able to cooperate temporally and spatially, leading to a stable flagellar waveform and swimming velocity, using a minimal representative computational model. Each dynein is subject to a periodic cycle along with a dynein-based switching mechanism, which is key to achieving dynein cooperation from any random initiation of dynein activity. We will show that an overall regular beating pattern emerges with time from an initially planar configuration due to the coordinated operation of the individual dyneins.

II. COMPUTATIONAL MODEL AND DIMENSIONAL ANALYSIS

A minimal representative model is used to study planar beating of natural flagella due to the coordinated operation of ATP-powered dyneins. The axoneme structure is modeled by two representative (doublet) microtubules that are connected via nexin links; see Fig. 4(a). A similar two-filament approach has been taken by Fauci and coworkers [35,40,41]. We analyze this system using a two-dimensional computational model in which an integral formulation for Stokes flow is implemented using the boundary element method to represent the fluid environment, while the microtubules and nexin links are represented by an assemblage of elastic beam elements. Each microtubule is discretized using 100 equal-sized beam elements and the analysis was carried out with a time-step of $0.1\,\mu$s, which assure numerical convergence of the results. The whole structure is embedded in an infinite fluid and the associated drag forces are computed using the Stokeslets approach. The solid mechanics and fluid dynamics equations are implicitly coupled using a finite element framework, details of which can be found in Appendix A [47]. We account for two groups of dyneins (groups A and B), each responsible for sliding (of the neighboring microtubules) in opposite directions; see Fig. 4(a). The dynein activity is shown in Fig. 4(a) by the vertical arrows, where the length of an arrow indicates the magnitude of the applied dynein force. Dyneins are found in many isoforms in an axoneme, which have distinct functions to facilitate flagellar motility [26,44]. Moreover, the spacing of these dyneins varies for outer- and inner-arm dyneins, while they retain a specific arrangement within the 96-nm repeat length of the outer doublet [45]. Here, we assume that all the dyneins are the same and are placed with a constant spacing; see Fig. 4(a). In the finite element implementation the sliding force of the dyneins F is transferred to the neutral axis of the beam, and equilibrium moments $M = 0.5F(d + l_{\text{nexin}})$ are introduced such that the loading system imposed by the dynein satisfies force and moment equilibrium; see Fig. 4(b). The dyneins are modeled as periodic force generators with an inherent duty ratio governed by the ATP hydrolysis cycle [23,24]. We assume that the dyneins will linearly increase the sliding force during their active phase (governed by t_a) until the stall force F_{stall} is reached, after which the dynein detaches and the force drops to zero during the recovery stroke (waiting phase) of the dyneins (governed by t_w); see Figs. 2 and 4(b). We link the ATP hydrolysis cycle to the dynein forcing cycle, represented by t_a, t_w, and F_{stall}, with F_{stall} being the maximum force a dynein molecule can apply, as obtained experimentally via optical-trap nanometry [23,25–28]. It should be noted that for computational efficiency we adopt a course-grained approach in which the number of dyneins present along the microtubules are captured in an average, smeared-out, manner. In Appendix B we have carried out discrete calculations with our ATP hydrolysis model and show that the collective behavior of multiple individual dyneins is in agreement with the experimentally observed sliding velocities observed in microtubule-motility assays.

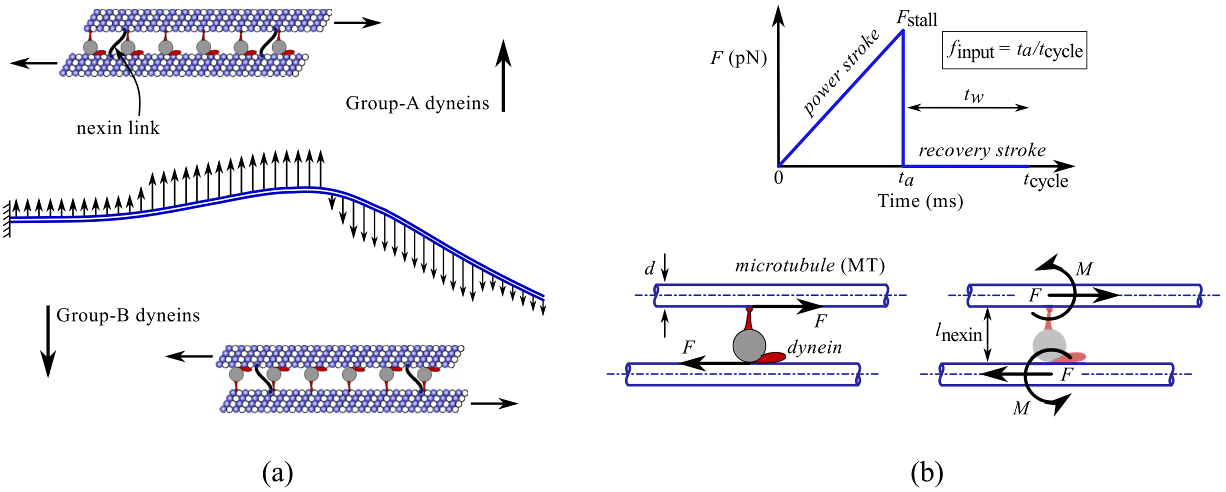

FIG. 4. (a) A representative computational model of the axoneme structure where two microtubules are connected via nexin links. Two groups (A and B) of dyneins are present at a regular spacing along the microtubules, each responsible for sliding in opposite directions. The dynein activity is shown by the vertical arrows, where the length of an arrow indicates the magnitude of the respective dynein force. Note that the actual dynein force is tangential to the axoneme. (b) The dynein force (F)—responsible for the relative sliding of the microtubules—is transferred to the neutral axis of the beam (representing the microtubules in the finite element model) and equilibrium moments are introduced, given by $M = 0.5F(d + l_{\text{nexin}})$, such that the loading system imposed by the dynein satisfies force and moment equilibrium. The dyneins are periodic force generators by linearly increasing the applied force (until the stall force F_{stall} is reached) during the power stroke (i.e., active period t_{a}) followed by a recovery ("waiting") period t_{w} in which the applied force remains zero. The dynein has an input duty ratio, $f_{\text{input}} = t_{\text{a}}/t_{\text{cycle}}$, where $t_{\text{cycle}} = t_{\text{a}} + t_{\text{w}}$, with the time periods depending on the ATP hydrolysis cycle [23,24].

We will study the flagellar beating pattern and swimming velocity as a function of the ATP-driven dynein cycle, the properties and structure of the axoneme, and finally, the viscosity of the fluid (μ). The dynein cycle is governed by t_a, t_w, and F_{stall}, and the axoneme structure is governed by the stiffness E of the microtubules, their vertical spacing H $(= d + l_{\text{nexin}})$, thickness d, and length L, and the stiffness E_{N} $(= E)$, thickness d_{N}, and horizontal spacing W of the nexin links; see Fig. 4(b). To efficiently explore the parametric space of the system, we will use the following set of dimensionless numbers. The dynein number,

$$D_{\text{n}} = m_{\text{stall}} L^2/Ed^3 = M_{\text{total}} L/Ed^3 = N_{\text{dyneins}} M_{\text{stall}} L/Ed^3, \tag{1}$$

the fluid number,

$$F_{\text{n}} = \mu L^3/t_a Ed^3, \tag{2}$$

the input duty ratio of the dyneins (governed by the ATP hydrolysis cycle),

$$f_{\text{input}} = t_a/t_{\text{cycle}}, \tag{3}$$

and the normalized length parameters,

$$d/d_{\text{N}}, H/L, \text{and}, W/L. \tag{4}$$

Here, $m_{\text{stall}} = M_{\text{total}}/L$ is the dynein moment-density (i.e., the total moment per unit length of the microtubule), $M_{\text{total}} = N_{\text{dyneins}} M_{\text{stall}}$ with N_{dyneins} being the total number of dyneins present along the length of a microtubule, and $M_{\text{stall}} = 0.5 F_{\text{stall}} H$ is the maximum moment (due to the stall force F_{stall}) of the dyneins per unit out-of-plane thickness, d_{N} is the thickness of the nexin links, and $t_{\text{cycle}} = t_a + t_w$. Note that we have two force parameters: (i) D_{n}, the ratio of applied dynein forces to elastic forces, and (ii) F_{n}, the ratio of viscous forces to elastic forces [46–49]. The input duty ratio f_{input} represents the intrinsically cyclic nature of the dyneins, the hydrodynamic interaction of two neighboring microtubules is governed by H/L, and W/L represents the number of nexin links.

The bending stiffness of the axonemal structure is quoted to be 4.2×10^{-22} Nm^2 [50], which is only one or two orders of magnitude higher than the reported bending stiffness of a microtubule (e.g., 1.9×10^{-24} Nm^2 [51,52] and 21.5×10^{-24} Nm^2 [53,54]), suggesting that the contribution of the nexin links to the effective bending stiffness of the axoneme is small, as also postulated in Ref. [14]. On the other hand, studies have also shown that nexin links can have an important contribution to the axoneme stiffness (see Refs. [55,56]). In the current paper, however, we neglect this effect by assuming that the nexin links are rather floppy relative to the microtubules by specifying $d/d_{\text{N}} = 100$, such that the bending stiffness of the system is dominated by the microtubule flexural stiffness. We assume the following dimensionless parameters in our simulations, unless specified otherwise: $D_{\text{n}} = 40$, $F_{\text{n}} = 53$, $f_{\text{input}} = 0.5$, $W/L = 0.01$, $H/L = 8.59 \times 10^{-3}$, $d/d_{\text{N}} = 100$.[3] We will refer to this case as the "reference" case.

III. RESULTS AND DISCUSSION

We start our computational analysis by exploring how the individual dyneins are able to generate an overall beat response

---

[3] This set of dimensionless numbers is on the same order of magnitude as that of realistic biological systems. For instance, $D_{\text{n}} = N_{\text{dyneins}} M_{\text{stall}} L/EI = 15$ and $F_{\text{n}} = \mu L^4/t_a EI = 32$ for $L = 40$ μm, $\mu = 1 \times 10^{-3}$ Pa.s, $EI = 4 \times 10^{-22}$ Nm^2, $t_a = 200$ ms, $F_{\text{stall}} = 2$ pN, $H = 90$ nm, $N_{\text{dyneins}} = 1666$ (assuming a 24-nm spacing).

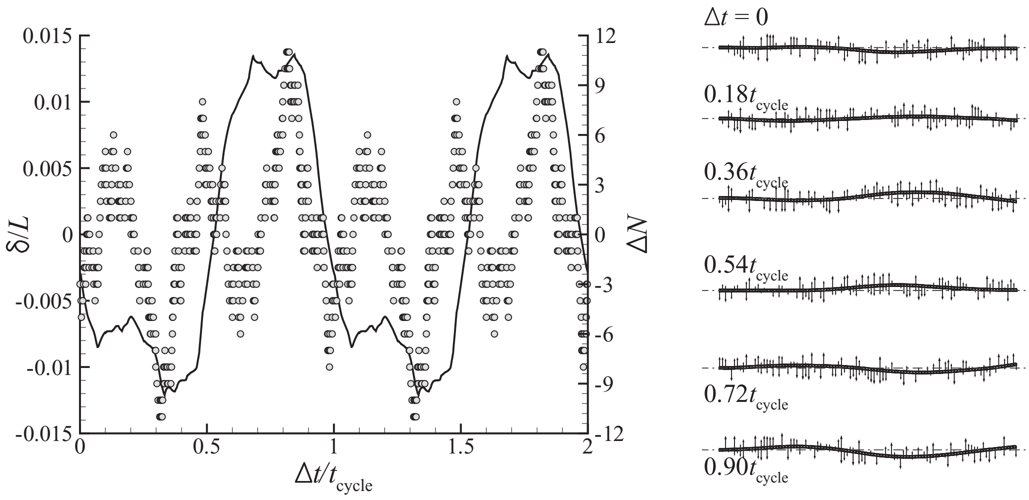

(a) (b)

FIG. 5. Steady-state response in the absence of a switching mechanism for the reference case. (a) Two groups of dyneins contribute to the axoneme deformation, where the normalized tip deflection, δ/L (left vertical axis), is indicated by the sold line, and the net number of active dyneins working at a time, $\Delta N = N_A - N_B$ (right vertical axis), is denoted by the symbols. Representative steady-state cycles are shown as a function of normalized time, $\Delta t/t_{\text{cycle}}$, with Δt representing the time elapsed during steady-state beating. (b) The dynein activity along the axonemal length with time is shown by the vertical arrows, where the length of an arrow indicates the magnitude of the respective dynein force (that is actually oriented tangential to the axoneme). Upward and downward arrows refer to the forces generated by the dyneins of group-A and group-B, respectively. The deflection amplitude remains low as the dyneins of the two different groups are competing with each other at a given cross-section.

for the situation depicted in Fig. 4(a) with clamped boundary conditions at the left end (i.e., both rotations and displacements are zero). At the start of the simulations a random time is assigned to each dynein from both groups, chosen from the ATP-driven working cycle between 0 and t_{cycle}, which places the dyneins either in an active state or in a waiting state. During the active state the dyneins cause relative sliding of the microtubules due to application of the sliding forces on the attached microtubules. Given that all the dyneins from both groups are the same, the overall deflection is governed by the effective number of dyneins, $\Delta N = N_A - N_B$, working along the length at a given time instance, leading to very small deflections δ of the right tip of the axoneme; see Fig. 5(a). Note that N_A and N_B are the total number of dyneins from group A and B, respectively, that are in the active phase, so that $\Delta N > 0$ corresponds to a tendency of the axoneme to deflect upward and $\Delta N < 0$ to deflect downwards [see Fig. 4(a)]. As the input duty ratio is an indication of the active number of dyneins at a given time instance, the average number of active dyneins for $f_{\text{input}} = 0.5$ will be 50%. However, in the absence of a switching mechanism the group A and B dyneins at each location can be operative at the same time [see Fig. 4(a)], so that the net number of active dyneins (ΔN) will be relatively low, as indicted by the symbols in Fig. 5(a). The dynein activity with time is shown in Fig. 5(b) by the vertical arrows, where the length of an arrow indicates the magnitude of the respective dynein force. Upward and downward arrows indicate dyneins in the active state of group-A and group-B, respectively. The deflection amplitude remains small due to the independent operation of both dynein groups A and B at each time instance and cross-section. We have also analyzed the case for $f_{\text{input}} = 0.9$ such that on average 90% of the dyneins are active. However, ΔN remains to be around 10 (10%), so that also for $f_{\text{input}} = 0.9$ the deflections remain small.

A. Dynein coordination and flagellar beating

Dyneins are minus-end directed motors, i.e., their power stroke is directed toward the minus-end of the microtubules [15], so that the natural sliding direction of groups A and B, are opposite to each other; see Fig. 4(a). In the absence of a switching mechanism, as studied in the previous subsection, the dyneins continue to apply force, even when sliding is opposite to their natural sliding direction. However, it has been postulated that during axonemal bending at a given cross-section one group of dyneins will experience positive sliding, while the second group, positioned diametrically opposite, will experience sliding in the opposite direction, which might trigger these second group of dyneins to switch-off [7,13]; see Fig. 3. We can look at this as a "negative-work-based deactivation" of the dyneins, which prompts an active dynein to go into the inactive state at the occurrence of sliding in the negative direction (i.e., opposite to its "natural" sliding direction). In addition, a persistent observation in theoretical and computational models is the fact that the applied forces and the development of curvature are out-of-phase [9,15,16,35–41], suggesting a time delay in the physical switching mechanism [8,9,15]. Indeed, theoretical studies on assemblies of motor proteins [57,58] have identified a time-delay between the action of the motor proteins and the response of the system. In addition, by studying the collective behavior of dyneins with load-dependent unbinding, a time-delay has been observed as well. In our work, we incorporate these observations by postulating a time-delay τ in our negative-work-based

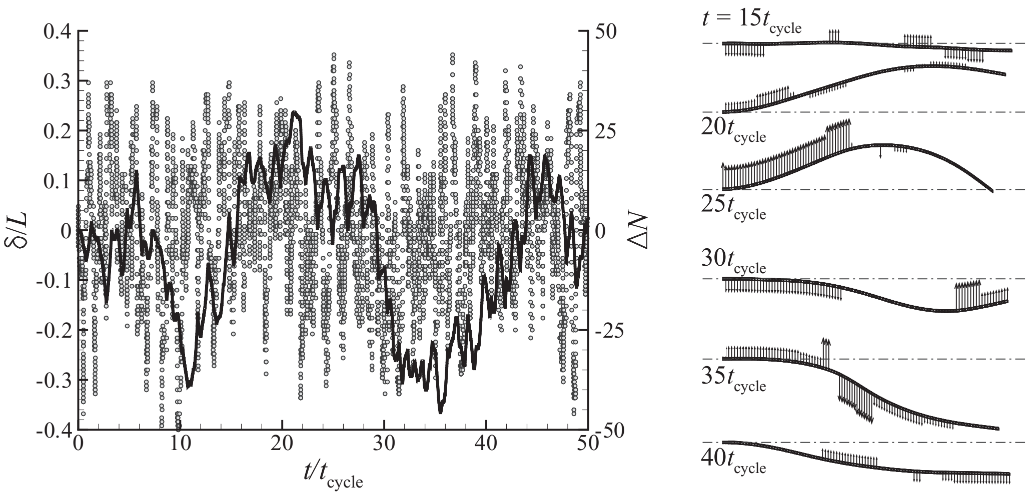

(a) (b)

FIG. 6. Axoneme deflection and dynein activity with time for the reference case with switching for $\tau = 0$, i.e., instantaneous deactivation of the dyneins at the occurrence of negative-work. (a) The normalized tip deflection, δ/L (left vertical axis), is indicated by the sold line, and the net number of active dyneins working at a time, $\Delta N = N_A - N_B$ (right vertical axis), is denoted by the symbols. (b) The dynein activity along the axonemal length with time is shown by the vertical arrows. Note, however, that the actual dynein force is oriented tangential to the axoneme. The large deflection of the axoneme is due to temporal regulation of the dynein activity, i.e., at any given cross-section only one group of dynein (either A or B) can be active at a given time instance.

deactivation mechanism. We will investigate the range of time delays between $\tau = 0$ (instantaneous switching) and $\tau = t_a$ (no switching, corresponding to Fig. 5).

We will first analyze the case of instantaneous switching ($\tau = 0$), the results of which are presented in Fig. 6. We observe that this negative-work-based deactivation of the dyneins facilitates a temporal regulation between group A and B, because this switching mechanism implicitly imposes the constraint that at any given cross-section of the axoneme only one dynein (either from group A or B) can be active at a given time instant, as shown in Fig. 6(b). A natural consequence is a significant increase in the effective number of dyneins (ΔN), which eventually leads to large deflection amplitudes, see Fig. 6(a), compared to the amplitudes in the absence of switching [see Fig. 5(a)]. However, as shown in Figs. 6(a) and 6(b), a steady-state behavior is not observed even after many cycles of ATP hydrolysis. The resulting motion appears to be primarily reciprocal, so that no directional swimming can be expected. Obviously, although the dyneins show temporal coordination, they are not able to spatially regulate their operation, which is key to break symmetry and to obtain nonreciprocal motion (wave propagation), leading to directional swimming.

Next, we investigate the effect of the time delay τ. For a time delay of $\tau/t_a = 0.2$, the axoneme deformation and dynein activity are shown in Fig. 7. We observe an emergence of dynein coordination (temporal as well as spatial) causing an evolution of local bend regimes in the axoneme and their propagation with time; see Fig. 7(b). The regular beating spontaneously emerges as a result of the switching mechanism (a time delayed deactivation of the dyneins based on negative work), imposed on an initially planar configuration of the axoneme with a spatially random distribution of (initial) dynein activity. Comparison of Figs. 7(a) and 5(a) shows that the effective number of dyneins (ΔN) now oscillates smoothly over a cycle time and that larger tip deflections are observed. The elastic deformation [indicated by δ in Fig. 7(a)] lags behind the actuation forces (the net force of the dyneins, proportional to ΔN) partly due to the delay and partly due to viscous drag, and the beat frequency is directly related to t_{cycle}; see Fig. 7(a).

The results so far have been obtained using clamped boundary conditions at the left end of the axoneme [see Fig. 4(a)]. Next, we release the swimmer and study the swimming response in the absence of constraining boundary conditions. The swimming displacement as a function of time is shown in Fig. 8(a) for six different realizations (i.e., these cases only differ by the random distribution of the initial dynein activity). For all the cases analyzed, the system requires approximately five ATP cycles before a steady state is settled in, leading to a constant swimming velocity. In addition, the results show that the swimming direction is not known *a priori* in our simulations and depends on the initial random placement of the dyneins in their respective working cycle. As the system evolves from an initial planar configuration to a flagellar waveform, the wave propagation can be toward the left or right with equal probability, since the flagellar beating patterns are the result of the emerging dynein coordination and is not enforced in the model. This is due to fact that the system is completely symmetric; there is no distinction between the basal and distal end of the axoneme, once the axoneme is unconstrained on both sides. Comparison of the clamped and free configuration shows that the dynein activity and wave characteristics remain mostly the same [see Figs. 7(a) and 8(b)]. We have also performed simulations on an intermediate case in which only the displacements were constrained, but the rotations were free. It was found that the boundary conditions do not significantly influence the emergent waveform, possibly due to the floppiness of the microtubules.

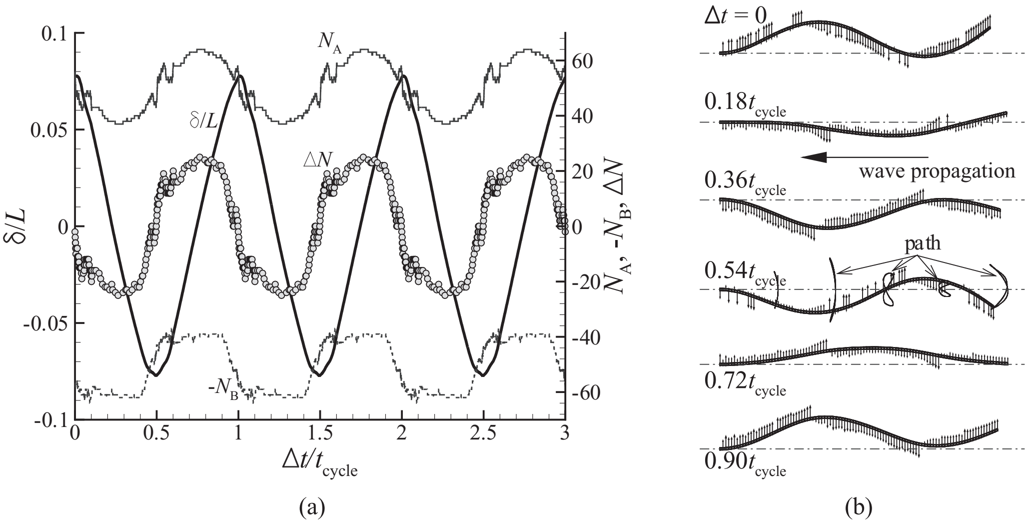

FIG. 7. Steady-state response for the reference case with switching for $\tau/t_a = 0.2$. (a) The effective number of active dyneins working at a time, $\Delta N = N_A - N_B$, is shown in comparison with the number of active dyneins of group A (N_A) and group B (N_B). The normalized tip deflection (δ/L) indicates the period of oscillations to be t_{cycle}, where representative steady-state cycles are shown as a function of $\Delta t/t_{\text{cycle}}$. (b) The dynein activity along the axonemal length with time is shown by the vertical arrows indicating the dynein coordination (temporal as well as spatial) causing an evolution of local bend regimes in the microtubules and their propagation with time. Note that the dynein force is oriented tangential to the axoneme.

The influence of the time delay, τ/t_a, on the swimming velocity and wave characteristics is shown in Fig. 9(a), where the absolute value of the swimming velocity U is normalized with L/t_{cycle}. Each data point corresponds to the average of ten different realizations. It is clear that a time-delayed deactivation of the dyneins based on negative work is necessary for emergence of dynein coordination leading to nonreciprocal motion and directional swimming. The swimming velocity increases sharply for low τ until it reaches a maximum around $\tau = 0.2t_a$. Since we allow the dyneins to do negative work for a period governed by τ/t_a, the dyneins are not working effectively for larger τ/t_a values, resulting in a decreasing velocity, which becomes zero for $\tau/t_a > 0.65$; see Fig. 9(a).

The value $\tau/t_a = 1$ corresponds to the case in which the switching mechanism is absent, resulting in simultaneous operation of both dynein groups, leading to small deflections and zero velocity as shown in Fig. 5. On the other hand, $\tau/t_a = 0$ causes instantaneous deactivation, which will lead to temporal coordination and large deflections, which however, do not result in spatial coordination nor make a transition to steady-state beating (see Fig. 6). Snapshots of steady-state swimming motion for $\tau/t_a = 0.2$ are shown in Fig. 9(b), where the curvature remains nearly constant as it propagates along the length of the axoneme, which is consistent with earlier findings [38,39]. Also, it is known that a nearly constant-curvature beating is characteristic for nonhyperactivated spermatozoa

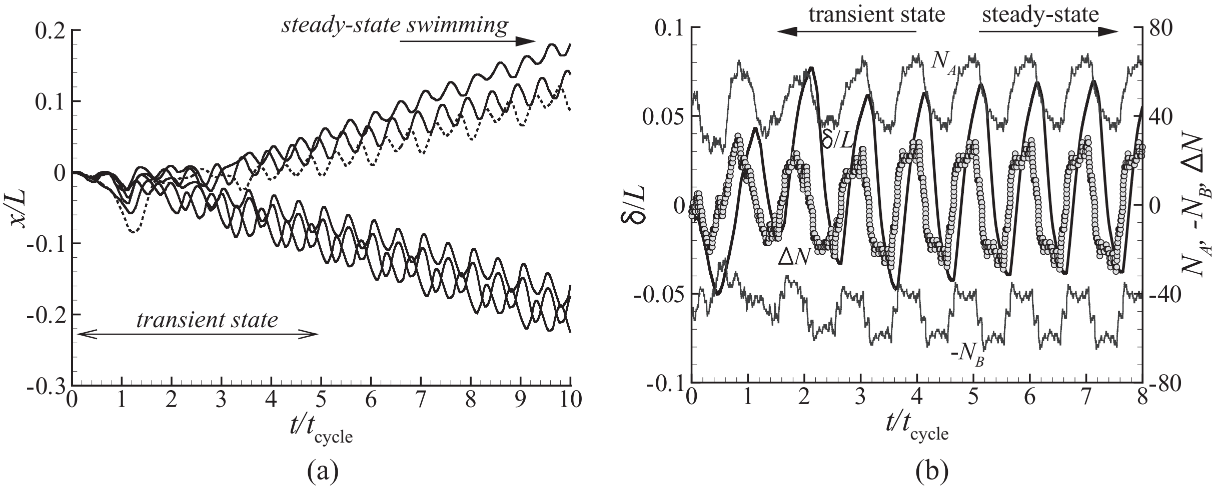

FIG. 8. Swimming response with switching for the reference case with $\tau/t_a = 0.2$. (a) The swimming displacement (x) with time indicating transient and steady-state swimming for six different realizations. (b) Axoneme deflection and dynein activity with time for a representative realization, which indicates that the steady-state beating emerges with time once the dynein activity stabilizes due to interference of the switching mechanism.

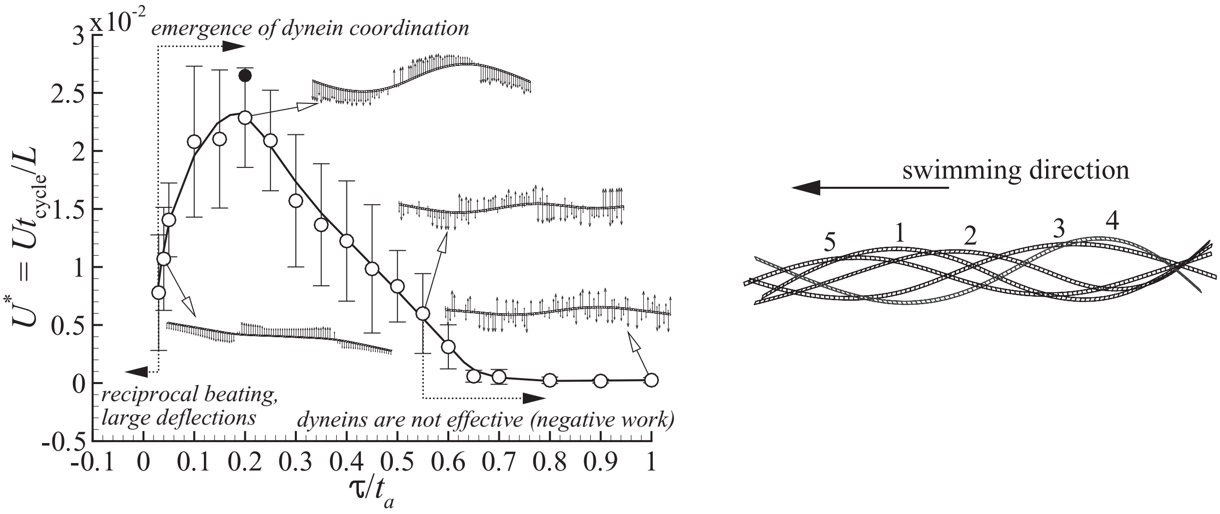

(a) (b)

FIG. 9. Steady-state swimming response with a time-delayed deactivation of the dyneins (based on negative work) for the reference case. (a) Normalized swimming velocity as a function of the normalized time delay for $0 \leqslant \tau \leqslant 1$. The swimming velocity increases sharply at the onset of wave propagation due to the emergence of dynein coordination. The value of $\tau/t_a = 0$ corresponds to instantaneous deactivation leading to reciprocal beating with large deflections, while $\tau/t_a = 1$ corresponds to the case in the absence of a switching mechanism. The error bars indicate the standard deviation of the results obtained by choosing ten different realizations. The filled symbol for $\tau/t_a = 0.2$ is for a partially uniform distribution of the dynein initiation time discussed in the text. (b) Snapshots of steady-state swimming motion for $\tau/t_a = 0.2$ with each snapshot (denoted by the numbers) separated by $t_{\text{cycle}}/5$. The curvature remains nearly constant as it propagates along the axoneme.

[59]. In Fig. 9(a) we show the general trend of the system using the data of ten different random distributions of the dynein initiation time. The computational cost of the analysis can be reduced by using a partially uniform distribution of the dynein initiation time, where we start our simulations by activating only a few dyneins of group A near the left end. The obtained results are within the statistical range, see the filled symbol for $\tau/t_a = 0.2$ in Fig. 9(a), and the axoneme deflection and dynein activity with time and space along the axoneme are similar to the cases obtained with a random initiation. We will use this partially uniform distribution for the dynein initiation in our further analysis.

B. The effect of stall force, viscosity, duty ratio, and deactivation time delay

In the following subsection we investigate the effect of the dimensionless numbers on the swimming velocity. We start our analysis by simulating the effect of D_{n} and F_{n}. There has been much debate on the specific value of the stall force for the axonemal dyneins and the presumably large difference in the force exerted by inner and outer dyneins [23,25–27]. The stall force enters in our analysis through the dimensionless "dynein" number D_{n}. In addition, the effect of viscosity on the flagellar beating characteristics has been often studied, showing that an increase of viscosity leads to a decrease in wavelength, deflection amplitude, and swimming velocity [35,39–41,60,61]. The viscosity enters in our analysis through the fluid number F_{n}. We study the influence of F_{n} for a given value of D_{n} (see Fig. 10). It can be seen from the insets of the right panel of Fig. 10 that an increasing F_{n} leads to a decrease in the wave length as well as the wave amplitude, which results in a decrease in the swimming velocity. This can be understood by referring to the well-known scaling relations for an infinitely long swimmer propagating a sinusoidal wave along its length [11,47,62–64]. Then, the swimming velocity is proportional to the square of the wave amplitude and inversely proportional to the wave length for small wave amplitudes. This indicates that the decreasing velocity with increasing F_{n} in Fig. 10 (right panel) is primarily due to the decrease in amplitude (despite the decrease in the wave length). In the left panel of Fig. 10, four flagellar waveforms are depicted (insets) for increasing values of both D_{n} and F_{n}. In that case, the wavelength decreases due to the increase in the fluid number F_{n}, while the decreasing amplitude due to F_{n} is compensated by the increase in D_{n}.

The influence of D_{n} on the swimming velocity is shown in Fig. 11 for various values of F_{n}. The results show that a considerable increase in the dynein force (D_{n}) is required to overcome the viscous drag forces represented by F_{n}. It can be seen that for a constant F_{n} value the wave amplitude is controlled by D_{n}; see the insets of Fig. 11. As D_{n} represents the ratio of the applied dynein forces to the elastic forces, an increasing D_{n} increases the wave amplitude, which causes a corresponding increase in the swimming velocity. The swimming velocity shows a quadratic dependence on D_{n} (for a given value of F_{n}), which can be seen from Fig. 11, where the solid lines are quadratic fits to the data. We have also studied the effect of the structural parameters H/L and W/L on the normalized swimming velocity. Their influence, however, was found to be negligible and will not be further discussed here. The interested readers are referred to Ref. [65].

We proceed to explore the influence of the input duty ratio f_{input} on the swimming velocity. The input duty ratio f_{input} is governed by the variation of ATP/ADP concentration in the aqueous environment. Experiments have shown that a decrease

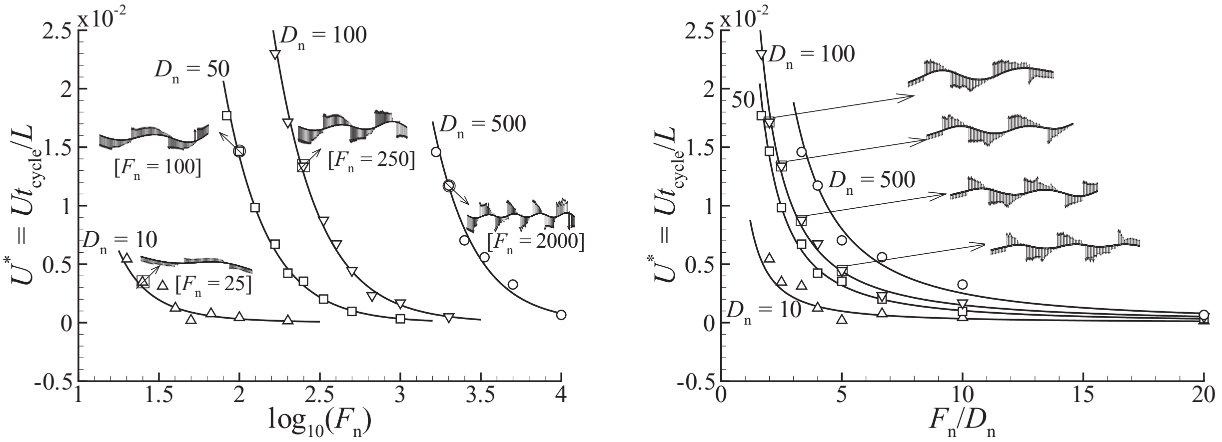

(a)

(b)

FIG. 10. Influence of F_n on the flagellar waveform and swimming velocity for $\tau/t_a = 0.2$ and $f_{\text{input}} = 0.5$ for different values of D_n (left panel). For a constant D_n value, F_n is observed to control the wave amplitude and the wave length (see the insets in the right panel), which results in a decrease in the swimming velocity. The insets in the left panel indicate the waveforms for four cases for increasing values of D_n and F_n. The thick solid lines are drawn only as a guide to the eye.

in the ATP concentration increases the total hydrolysis time, t_{cycle} as well as f_{input} [3]. Similarly, the ADP concentration might affect the release of ADP and thus the time scales of the power stroke (see Fig. 2). Indeed, observations on the reaction kinetics indicate that the product release (Pi and ADP) is the rate-limiting reaction during the ATP hydrolysis cycle [24]. To explore the effect of f_{input} we vary the activation time t_a at constant cycle time t_{cycle}; see Fig. 12. As a result, also τ/t_a will change for a constant value of τ, which has been shown to have an important effect on the swimming velocity [see Fig. 9(a)]. The results indicate that the swimming velocity depends on the value of τ/t_a and is maximum for $f_{\text{input}} = 0.5$ (see Fig. 12) as shown earlier in Fig. 9(a). The swimming velocity is maximal for $f_{\text{input}} = 0.5$ and for $f_{\text{input}} > 0.5$ a decrease in the swimming velocity is observed. For $f_{\text{input}} < 0.5$ the dyneins will have less time to be active (additionally, there will be an increase in the τ/t_a value when τ is constant), which causes the swimming velocity to decrease.

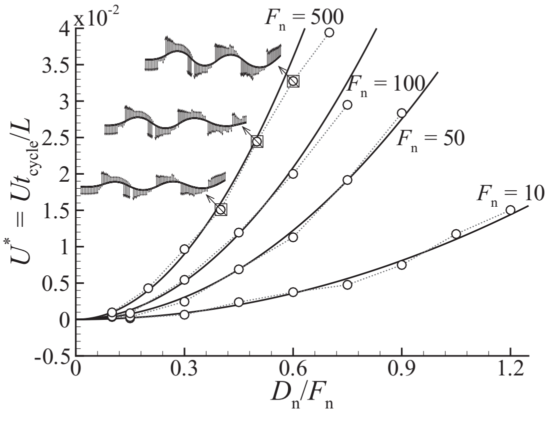

FIG. 11. Influence of D_n on the flagellar waveform and swimming velocity for $\tau/t_a = 0.2$ and $f_{\text{input}} = 0.5$ for different values of F_n. For a constant F_n value, D_n is observed to control the wave amplitude (see the insets), which leads to a corresponding increase in the swimming velocity. The thick solid lines are quadratic fits to the data.

Interestingly, the beat frequency is found to depend on the maximum value of t_{cycle} and $2t_a$, so that $t_{\text{beat}} = t_{\text{cycle}}$ for $f_{\text{input}} \leqslant 0.5$ and $t_{\text{beat}} = 2t_a$ for $f_{\text{input}} > 0.5$. Once we normalize the swimming velocity with the time period of the flagellar beat (t_{beat}) instead of t_{cycle}, the swimming velocity appears to be independent of f_{input} for values greater than 0.5 [65].

The beating frequency of the flagellum (t_{beat}) intrinsically depends on the period associated with the ATP hydrolysis cycle. In our model, t_a and t_{cycle} do not depend on the viscosity, leading to $t_{\text{beat}} = 2t_a = t_{\text{cycle}}$ for $f_{\text{input}} = 0.5$. However, as discussed in the first paragraph of this section, the model captures the influence of the fluid viscosity on the wave amplitude, wave length, and resulting swimming velocity, which are in qualitative agreement with earlier observations [35,39–41,60,61]. Interestingly, in an experimental study by Ishijima and Hiramoto [50] the beating frequency remains unchanged with increasing viscous forces imposed by an additional fluid flow in the direction of bend propagation [15]. Furthermore, it is known that the ATP concentration will affect

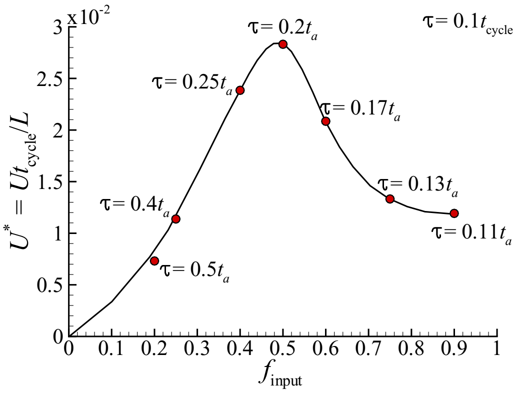

FIG. 12. Influence of f_{input} on the swimming velocity for a constant cycle time t_{cycle}.

the flagellar beating frequency [60] and dynein stall force [28]. In our model, the input duty ratio f_{input} and associated time periods t_a and t_{cycle} are governed by the ATP concentration. For instance, decreasing t_{cycle} in our model to incorporate an increase in the ATP concentration [23,24] will increase the resulting beat frequency (see, e.g., Figs. 7 and 8), as also observed in flagellar studies [66].

IV. SUMMARY AND CONCLUSIONS

We have computationally analyzed the planar beating of natural flagella powered by ATP-driven dyneins using a two-dimensional finite element framework in which the solid mechanics and fluid dynamics equations are solved simultaneously. We consider a minimal representative model in which the axoneme structure is represented by two microtubules that are connected via nexin links. Flagellar beating emerges due to the interaction of two groups of dyneins, each responsible for sliding in opposite directions, in the presence of a switching mechanism. The dyneins are modeled as periodic force generators represented by the stall force, duty ratio, and cycle time, which are related to the power and recovery stroke of a dynein molecule during its ATP-driven hydrolysis cycle. The dyneins are deactivated at the end of the (active) cycle or when negative work is done during the cycle. Our results show that a time delay between the occurrence of negative work and deactivation is key in generating nonreciprocal motion leading to swimming. A stable flagellar waveform and beating pattern emerges from an initially planar microtubule configuration starting from a random distribution of dynein activity in their ATP hydrolysis cycle. We have identified the key dimensionless parameters responsible for flagellar beating and have explored the associated system response. The influence of the stall force of the dyneins is captured by the dynein number, which is responsible for the magnitude of the wave amplitude. The influence of the fluid viscosity is captured by the fluid number, which controls the wave length as well as the wave amplitude. The influence of the ATP/ADP concentration is captured by the ATP hydrolysis cycle time and input duty ratio, which control the beating frequency. The simulation results are in qualitative agreement with the experimental observations. These findings might provide insights on the fundamental working mechanism of axonemal dyneins, and possibly will open new research directions in the field of flagellar motility.

ACKNOWLEDGMENTS

We acknowledge the Dutch Polymer Institute (DPI) for funding under Project Code DPI-699 (ARTFLAG).

APPENDIX A: A COMPUTATIONAL FRAMEWORK FOR FLAGELLAR PROPULSION[4]

To solve the coupled fluid-structure interaction (FSI) problem, we utilize the principle of virtual work containing all the relevant energies and adopt an updated Lagrangian framework to arrive at the final set of equations. By implicitly coupling the solid mechanics and fluid dynamics equations, we incorporate the equivalent drag matrix due to the fluid into the stiffness matrix while solving the equations of motion for the FSI problem [47].

1. Finite element formulation of the solid dynamics equations

The principle of virtual work for the system under consideration can be written on the undeformed configuration as

$$\int_{V_0} \sigma \delta \epsilon dV - \int_{S_0} (\delta \boldsymbol{u})^T \boldsymbol{T}_d dS = 0, \tag{A1}$$

where σ is the stress at point (x,y) and $\boldsymbol{T}_d = \{T_u, T_v\}^T$ is the traction vector due to viscous forces of the fluid (see Fig. 13). The deformation of a 2D beam structure can be described in terms of the axial and transverse displacements of its axis, $\boldsymbol{u} = \{u,v\}^T$. The characteristic strains, given by the axial strain $\overline{\epsilon}$ and the curvature κ, contribute to the Lagrange strain ϵ as

$$\epsilon = \frac{du}{dx} + \frac{1}{2}\left(\frac{dv}{dx}\right)^2 - y\frac{d^2v}{dx^2} \quad = \quad \overline{\epsilon} - y\kappa. \tag{A2}$$

For a beam of uniform cross-section with thickness h and out-of-plane thickness of unity, we can write

$$\int_x (P\delta\overline{\epsilon} + M\delta\kappa)dx - \int_x (\delta\boldsymbol{u})^T \boldsymbol{T}_d dx = 0, \tag{A3}$$

where $P = \int_y \sigma dy$ and $M = -\int_y \sigma y dy$ [67]. The virtual work equation at time $t + \Delta t$ can be written as

$$\int_x (P^{t+\Delta t}\delta\overline{\epsilon}^{t+\Delta t} + M^{t+\Delta t}\delta\kappa^{t+\Delta t})dx$$
$$- \int_x (\delta\boldsymbol{u}^{t+\Delta t})^T \boldsymbol{T}_d^{t+\Delta t} dx = 0, \tag{A4}$$

which can be expanded linearly in time by assuming $Q^{t+\Delta t} = Q^t + \Delta Q$ and can be simplified by neglecting the higher-order terms, leading to

$$\int_x \left(P^t\delta\overline{\epsilon}^t + M^t\delta\kappa^t + \Delta P\delta\overline{\epsilon}^t + \Delta M\delta\kappa^t + P^t\Delta\delta\overline{\epsilon}\right)dx$$
$$- \int_x (\delta\boldsymbol{u}^{t+\Delta t})^T \boldsymbol{T}_d^{t+\Delta t} dx = 0. \tag{A5}$$

We use the finite element formulation to discretize the system in terms of the nodal displacements and rotations $\boldsymbol{d}_e$

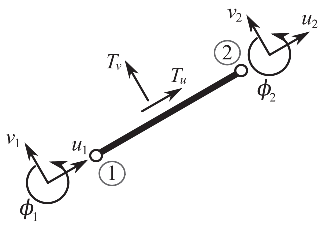

FIG. 13. A representative finite element with the corresponding nodal degrees of freedom (u,v,ϕ) subjected to the external traction forces (T_u,T_v) due to the surrounding fluid.

---

[4] Reproduced from Namdeo *et al.*, Biomicrofluidics **5**, 034108 (2011) with the permission of AIP Publishing.

of the Euler-Bernoulli beam elements (see Fig. 13) with $\boldsymbol{d}_e = \{u_1, v_1, \phi_1 l_r, u_2, v_2, \phi_2 l_r\}^T$, where $u_i, v_i, \phi_i, i = 1,2$, denote the nodal displacements and rotation of the element in nodes 1 and 2, respectively, and l_r is a reference length chosen to be the total length of the microswimmer (L) in the present analysis. The axial displacements are linearly interpolated while the transverse displacements are cubically interpolated,

$$u = \boldsymbol{N}_u \boldsymbol{d}_e, \quad v = \boldsymbol{N}_v \boldsymbol{d}_e, \tag{A6}$$

where $\boldsymbol{N}_u$ and $\boldsymbol{N}_v$ being the standard interpolation matrices [68]. Now, using the standard finite element notations $du/dx = \boldsymbol{B}_u \boldsymbol{d}_e$, $dv/dx = \boldsymbol{B}_v \boldsymbol{d}_e$, $d^2u/dx^2 = \boldsymbol{C}_v \boldsymbol{d}_e$, and constitutive relations $\Delta P = Eh\Delta\bar{\epsilon}$, $\Delta M = EI\Delta\kappa$, with E being the elastic modulus and I being the second moment of inertia given as $I = h^3/12$, the discretized virtual work equation can be written as

$$\boldsymbol{K}_e^t \Delta \boldsymbol{d}_e + \boldsymbol{f}_{\text{int}}^t - \boldsymbol{f}_{\text{ext}}^{t+\Delta t} = 0, \tag{A7}$$

where $\boldsymbol{K}_e$ is the elemental stiffness matrix, $\boldsymbol{f}_{\text{int}}$ is the internal nodal force vector, and $\boldsymbol{f}_{\text{ext}}$ is the external nodal force vector due to the drag forces of the fluid, which can be written as

$$\boldsymbol{K}_e^t = \int_x \left(Eh\boldsymbol{B}_u^T \boldsymbol{B}_u + EI\boldsymbol{C}_v^T \boldsymbol{C}_v + P^t \boldsymbol{B}_v^T \boldsymbol{B}_v\right) dx,$$

$$\boldsymbol{f}_{\text{int}}^t = \int_x \left(P^t \boldsymbol{B}_u^T + M^t \boldsymbol{C}_v^T\right) dx, \quad \text{and}$$

$$\boldsymbol{f}_{\text{ext}}^{t+\Delta t} = \int_x \boldsymbol{N}^T \boldsymbol{T}_d^{t+\Delta t} dx,$$

in which $\boldsymbol{N}$ consists of the shape functions $\boldsymbol{N}_u$ and $\boldsymbol{N}_v$ and the domain of integration was chosen to be the deformed configuration (updated Lagrangian framework, $\boldsymbol{d}_e = 0$). Finally, the equations of motion can be written after the finite element assembly as

$$\boldsymbol{K}^t \Delta \boldsymbol{d} + \boldsymbol{F}_{\text{int}}^t - \boldsymbol{F}_{\text{ext}}^{t+\Delta t} = 0. \tag{A8}$$

The external forces $\boldsymbol{F}_{\text{ext}}$ consist of tractions imposed by the fluid and are calculated using a 2D Stokeslet approach as described in the following sections.

2. Boundary element formulation of the fluid dynamics equations

For the fluid we make use of the Stokeslet approach in which the force exerted on the fluid at the surface of the solid structure is approximated by the distribution of Stokeslets along the length of the structure. The velocity and force fields are related by a Green's function that has a singularity proportional to $1/r$ in three dimensions and $\ln(r)$ in two dimensions [69]. The expression of Green's function ($\boldsymbol{G}$) for the Stokeslets relates the velocity at location $\boldsymbol{r}$, $\dot{\boldsymbol{u}}$, to the forces at location $\boldsymbol{r}\prime$, $\boldsymbol{f}$, through

$$\dot{\boldsymbol{u}} = \boldsymbol{G}\boldsymbol{f} \quad \text{and} \quad G_{ij} = \frac{1}{4\pi\mu}\left\{-\ln(R)\delta_{ij} + \frac{R_i R_j}{R^2}\right\} \quad \text{for} \quad (i,j = 1,2), \tag{A9}$$

where $\boldsymbol{R} = \boldsymbol{r} - \boldsymbol{r}\prime$, $R = |\boldsymbol{R}|$ is the distance between the two locations $\boldsymbol{r}$ and $\boldsymbol{r}\prime$ and δ_{ij} is the Kronecker δ. By assuming the point force $\boldsymbol{f}$ to be represented by the traction $\boldsymbol{f} = \boldsymbol{T}dS$ over the solid surface, the boundary-integral equation can be written as

$$\dot{\boldsymbol{u}} = \int_{\text{boundary}} \boldsymbol{G}\boldsymbol{T}dS = \sum_{\text{nelm}} \int_{L_e} \boldsymbol{G}\boldsymbol{T}dS = \sum_{\text{nelm}} \int_{L_e} \boldsymbol{G}\boldsymbol{N}dS\boldsymbol{t}, \tag{A10}$$

where $\boldsymbol{T}$ are the tractions imposed on the fluid and $\boldsymbol{T} = -\boldsymbol{T}_d$. In Eq. (A10), the boundary-integral equation has been discretized using boundary elements of length L_e, and the tractions are linearly interpolated using $\boldsymbol{T} = \boldsymbol{N}\boldsymbol{t}$ with $\boldsymbol{t}$ being the tractions at the nodes. When Eq. (A10) is used to evaluate the velocity in all nodes of the flagellum, we obtain a system of equations $\dot{\boldsymbol{U}} = \boldsymbol{G}_f \boldsymbol{t}$ that relates the traction $\boldsymbol{t}$ exerted by the flagellum on the fluid to it's velocity $\dot{\boldsymbol{U}}$. The integration procedure is adopted from the literature [69]. Once the velocity of the solid surface is known, this relation can be inverted to obtain the nodal tractions: $\boldsymbol{t} = \boldsymbol{G}_f^{-1}\dot{\boldsymbol{U}}$.

3. Fluid-solid interaction and implicit coupling

Coupling of the solid mechanics and fluid dynamics equations will be done in an implicit manner by incorporating the equivalent drag matrix due to the fluid into the stiffness matrix [70]. The external nodal force vector due to the fluid's drag forces [see Eq. (A7)] can be given as

$$\boldsymbol{f}_{\text{ext}}^{t+\Delta t} = \int_x \boldsymbol{N}^T \boldsymbol{T}_d^{t+\Delta t} dx = -\int_x \boldsymbol{N}^T \boldsymbol{N} dx \;\; \boldsymbol{t}^{t+\Delta t} = -\boldsymbol{M}_e \boldsymbol{t}^{t+\Delta t}, \tag{A11}$$

where $\boldsymbol{M}_e = \int_x \boldsymbol{N}^T \boldsymbol{N} dx$ in which we only consider the linear shape functions for $\boldsymbol{N}$. Note that the minus sign appears due to the change of reference (from fluid to the structure, $\boldsymbol{T}_d = -\boldsymbol{T}$). After performing the standard finite element assembly procedure we get

$$\boldsymbol{F}_{\text{ext}}^{t+\Delta t} = -\boldsymbol{M}\boldsymbol{t}^{t+\Delta t} = -\boldsymbol{M}\boldsymbol{G}_f^{-1}\dot{\boldsymbol{U}}^{t+\Delta t}, \tag{A12}$$

where the matrix $\boldsymbol{G}_f$ relates the velocity of the solid structure to the traction, see Appendix A.2. Now, using the no-slip boundary condition $\dot{\boldsymbol{U}} = \boldsymbol{A}\Delta\boldsymbol{d}/\Delta t$, it follows that

$$\boldsymbol{F}_{\text{ext}}^{t+\Delta t} = -\boldsymbol{M}\boldsymbol{G}_f^{-1}\boldsymbol{A}\Delta\boldsymbol{d}/\Delta t = -\boldsymbol{K}_D^t \Delta\boldsymbol{d}, \tag{A13}$$

where $\boldsymbol{K}_D = \boldsymbol{M}\boldsymbol{G}_f^{-1}\boldsymbol{A}/\Delta t$ is an equivalent drag matrix and is the stiffness contribution due to the presence of the fluid. $\boldsymbol{A}$ is a matrix that eliminates the rotational degrees of freedom from the global displacement vector $\Delta\boldsymbol{d}$. After incorporating the appropriate boundary conditions, we will be solving the following equation of motion for the FSI problem to obtain the incremental displacements ($\Delta\boldsymbol{d}$):

$$\left\{\boldsymbol{K}^t + \boldsymbol{K}_D^t\right\}\Delta\boldsymbol{d} = -\boldsymbol{F}_{\text{int}}^t. \tag{A14}$$

This appendix has been reproduced from Ref. [47], with the permission of AIP Publishing.

APPENDIX B: MOLECULAR STUDIES ASSOCIATED WITH AXONEMAL DYNEINS

To study the flagellar beating we have used a representative and coarse-grained model, where the number of dyneins present along the microtubules are captured in an average sense. Experimental molecular studies point to the stepping behavior of the dynein molecules, where a limited step size of 8–24 nm is usually observed for axonemal dyneins per ATP hydrolysis cycle [23,25–28]. In the following we will confront our dynein model to the molecular studies associated with axonemal dyneins based on optical-trap nanometry and microtubules-motility assay by properly accounting for the step size of a dynein molecule. We account for the step size for every dynein in our model by monitoring the net sliding displacement during the active phase of a dynein. Once the sliding displacement exceeds the maximum step size, the dynein in question is deactivated.

In experimental studies researchers have analyzed the force-transduction of individual dynein molecules with optical-trap nanometry [23,25–28]. Optical-trap nanometry utilizes the gradient force of a highly focused laser beam (optical-trap) to monitor the forces exerted by a dynein-coated bead on a substrate coated with microtubules [27]. The experimental conditions are optimized and controlled in such a way that only one dynein molecule (along the bead surface) is interacting with a microtubule at a given time instant [27]. This dynein-microtubule interaction and cyclic conformational change of the dynein molecule—associated with the ATP hydrolysis—leads to the guided translocation of the bead over the microtubule. In the absence of any resistance from the optical-trap the unloaded translocation velocity of the bead due to the dynein activity can be obtained. Moreover, once the bead motion is influenced by the optical-trap, the step-wise motion of the bead with time can be observed, which gives information on the step size of the dynein molecule during a binding and power stroke, and the maximum force at which the dynein motion is stalled (the stall force) [23,25–27].

To relate our dynein model to the optical-trap nanometry experiments, we use a representative model where a dynein is periodically interacting with a neighboring microtubule leading to sliding, while the motion of the microtubule is restrained via a soft spring, as shown in the inset of Fig. 14(a). The length of the microtubule is selected to approximate the drag forces of the micron-sized bead used during the optical-trap experiments. We assume that one dynein is constantly interacting with the neighboring microtubule to replicate the experimental conditions. The resulting stepping behavior of the dyneins is shown in Fig. 14(a). It can be noted that due to the periodic dynein-to-microtubule interaction the sliding displacement increases until the point where the restoring force of the spring is in equilibrium with the dynein's applied sliding force. This gives the maximum sliding displacement ($\delta_{\max}$) possible for a given stall force of the dynein (F_{stall}) and stiffness of the spring (K_{trap}), $F_{\text{stall}} = K_{\text{trap}}\delta_{\max}$. The stepping behavior of a dynein per hydrolysis cycle is visible as the dynein gets deactivated once it exceeds the step size (δ_{step}) during the early stage of the analysis; see Fig. 14(a). After deactivation, the applied dynein force resets to zero, so that the restoring force of the spring pulls the microtubule backwards (indicated by the periodic decrease in the displacement), which is limited by the viscous drag. Followed by this brief event, the dynein again attaches itself to the microtubule (i.e., another dynein in the dynein-coated bead in the experiments) and again starts applying the sliding force, which overcomes the spring force and slides the microtubule forward; see Fig. 14(b). The time history of the applied force by the dynein and the resulting stepping behavior is shown in Fig. 14(b). The stepping behavior of the dynein also depends on the magnitude

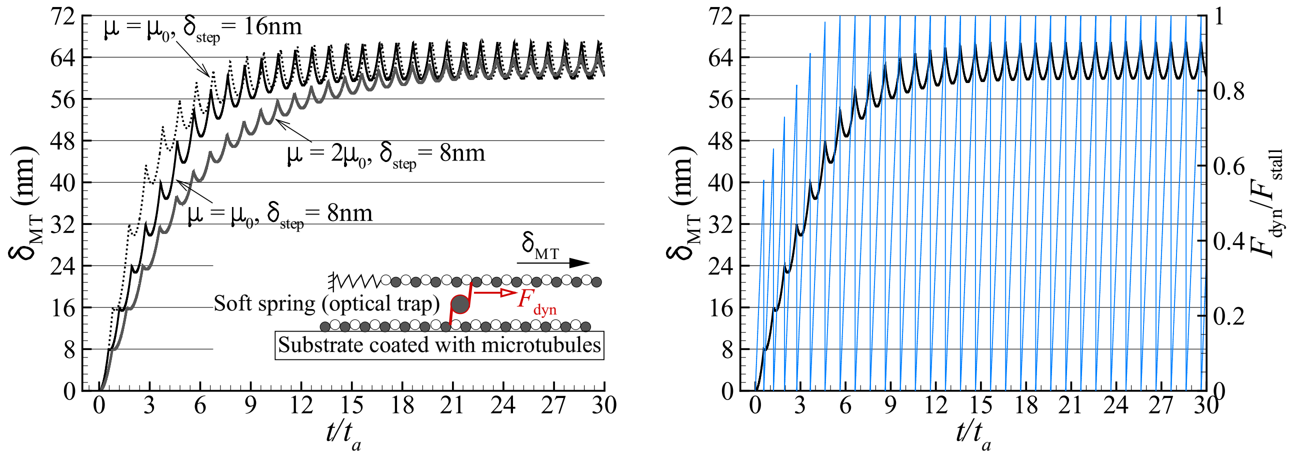

(a)

(b)

FIG. 14. (a) Influence of the fluid viscosity and the step size on the stepping behavior of the dyneins subjected to the restraining action of the attached spring representing the experimental conditions for optical-trap nanometry (see the inset). Note that the motion of the bead is stalled when the applied force of the dynein is in an equilibrium with the restoring force of the spring, which appears to be independent of the step-size and fluid viscosity. (b) The time history of the resulting applied force by the dynein and resulting stepping behavior for $\delta_{\text{step}} = 8$ nm and $\mu = \mu_0 = 0.48$ mPa.s with the assumption that one dynein is constantly interacting with the neighboring microtubule, where the thin line represents the dynein force.

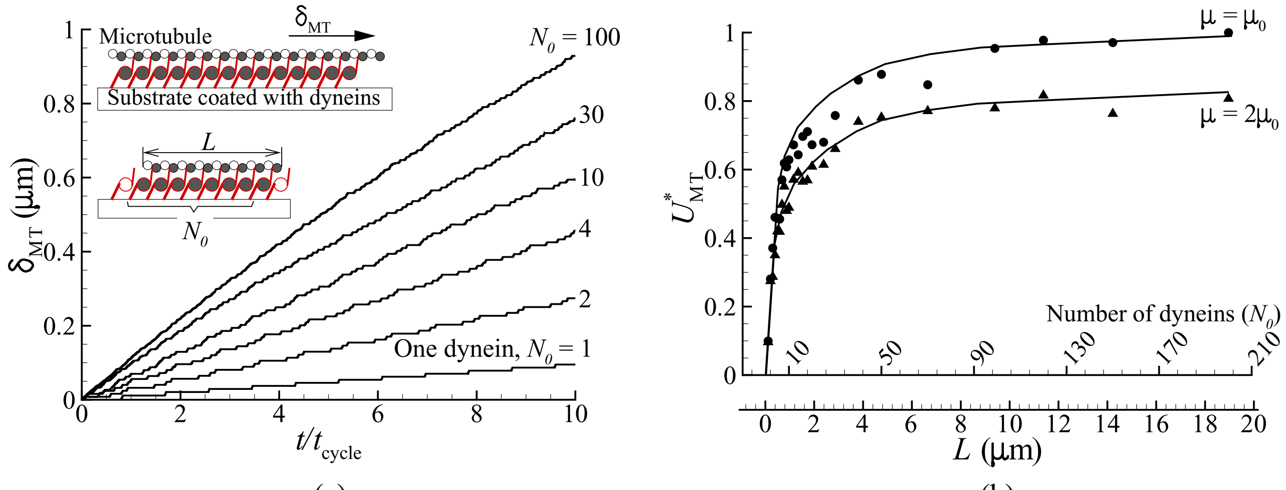

(a) (b)

FIG. 15. (a) Influence of the microtubule length (or number of dyneins, N_0) on the resulting sliding displacement due to the dynein activity ($\mu = \mu_0$). To represent the experimental conditions related to the microtubules-motility assay dyneins are placed with a constant interspacing (96 nm) over the substrate, which limits the maximum number of dyneins (N_0) that can interact with a microtubule of length L as shown in the inset. (b) The sliding velocity with length of the microtubule, which also quantifies the number of dyneins (possibly) interacting with the microtubules. The sliding velocities are normalized such that the maximum sliding velocity is $U^*_{MT} = 1$ for $\mu = \mu_0$. The data points are obtained via simulations, where dyneins have a low duty ratio $f_{dynein} = 0.15$ and a step size of 8 nm is used. The solid lines are the fitted trend that is in agreement with the statistical expression relating the number of dyneins and their duty ratio to an expected sliding velocity of the microtubule (see the main text).

of the restoring force and it can be seen from Fig. 14(a) that the step size becomes smaller as the magnitude of the restoring force approaches the stall force.

To understand the collective behavior of the dyneins and their interaction with the neighboring microtubules, various microtubule-motility and gliding assay experiments were carried out [25,29–34]. In these gliding assay experiments, many dyneins coated on the substrate are interacting with (isolated) microtubules of various lengths [29,32]. The dynein-microtubule interaction and the cyclic conformational change of the dynein molecule leads to guided translocation of the microtubules over the substrate. The sliding velocity of the microtubules has been found to increase with the length of the microtubules until a saturation velocity (U_{max}) is reached for large microtubule lengths [29,32]. As the number of dyneins that can interact with a microtubule is limited by the length of the microtubule itself (due to the regular spacing of the dyneins), the sliding velocity increases due to the increasing number of interacting dyneins [29–32]. A step-size at the nanometer scale during the time period of a few milliseconds (typical for the ATP hydrolysis cycle) will lead to a microtubule velocity on the order of a few micrometers per second, as observed experimentally [27].

To explore the microtubule sliding velocity due to the operation of many dyneins, we use a representative model where dyneins are interacting with a free or isolated microtubule; see the inset of Fig. 15(a). The number of dyneins interacting with the microtubule is altered by changing the length of the microtubule, as dyneins are present with a constant spacing. In the simulations, we alter the microtubule length (which can be correlated with the number of dyneins, N_0) to study the resulting sliding velocity. Only one group of the dyneins is considered to replicate the experimental situation, where only one family attaches to the microtubule as dyneins are unidirectional motors. We assume here that the dyneins have a low duty ratio ($f_{dynein} = 0.15$) and we account for the step size per hydrolysis cycle ($\delta_{step} = 8$ nm) of a dynein molecule. Due to the dynein activity, the microtubule moves forward and once the dynein is deactivated (either due to the end of the active phase or due to reaching the maximum step size), the microtubule remains in the same position until the next dynein becomes active; see Fig. 15(a). A saturation in the resulting sliding velocity is observed with the length of the microtubule, see Fig. 15(b), which is in accordance with the experimental observations [29–32]. The sliding velocity due to just one dynein can be theoretically approximated (without accounting for the viscosity) by δ_{step}/t_{cycle}, while the maximum sliding velocity $U_{max} = \delta_{step}/t_a$, which represents the condition that the maximum sliding velocity is limited by the rate of conformation change responsible for the dynein power stroke. However, in order to attain the maximum sliding velocity at least one dynein should be active at all times, as can be clearly seen from the microtubule displacement caused by the dynein activity in Fig. 15(a). Obviously, as we increase the number of dyneins the probability of at least one dynein to be active at all times increases, and can be quantified with $1-(1-f_{dynein})^N$ for N number of dyneins with a duty ratio, f_{dynein}. Moreover, a statistical expression can be obtained relating the number of dyneins and their duty ratio to an expected sliding velocity of the microtubule, $U_{MT} = U_{max}[1-(1-f_{dynein})^N]$, where U_{max} is the maximum sliding velocity observed at the saturation [29].

[1] M. A. Sleigh, *Cilia and Flagella* (Academic Press, London/New York, 1974).
[2] H. Lodish, A. Berk, S. L. Zipursky, P. Matsudaira, D. Baltimore, and J. Darnell, *Molecular Cell Biology*, 4th ed. (W. H. Freeman, New York, 2000).
[3] S. A. Burgess, M. L. Walker, H. Sakakibara, P. J. Knight, and K. Oiwa, Dynein structure and power stroke, Nature **421**, 715 (2003).
[4] S. A. Burgess and P. J. Knight, Is the dynein motor a winch? Curr. Opin. Struct. Biol. **14**, 138 (2004).
[5] A. J. Hunt, Molecular motors: Keeping the beat, Nature **393**, 624 (1998).
[6] H. Ueno, T. Yasunaga, C. Shingyoji, and K. Hirose, Dynein pulls microtubules without rotating its stalk, Proc. Natl. Acad. Sci. USA **105**, 19702 (2008).
[7] T. J. Mitchison and H. M. Mitchison, Cell biology: How cilia beat, Nature **463**, 308 (2010).
[8] C. B. Lindemann and K. A. Lesich, Flagellar and ciliary beating: The proven and the possible, J. Cell Sci. **123**, 519 (2010).
[9] C. J. Brokaw, Thinking about flagellar oscillation, Cell Motil. Cytoskeleton **66**, 425 (2009).
[10] S. Camalet and F. Jülicher, Generic aspects of axonemal beating, New J. Phys. **2**, 24 (2000).
[11] E. Lauga and T. R. Powers, The hydrodynamics of swimming microorganisms, Rep. Prog. Phys. **72**, 096601 (2009).
[12] M. Murase, Simulation of ciliary beating by an excitable dynein model: Oscillations, quiescence, and mechano-sensitivity, J. Theor. Biol. **146**, 209 (1990).
[13] K. Inaba, Sperm flagella: Comparative and phylogenetic perspectives of protein components, Mol. Human Repro. **17**, 524 (2011).
[14] Riedel-I. Kruse, A. Hilfinger, J. Howard, and F. Jülicher, How molecular motors shape the flagellar beat, HFSP J. **1**, 192 (2007).
[15] D. M. Woolley, Flagellar oscillation: A commentary on proposed mechanisms, Biol. Rev. **85**, 453 (2010).
[16] K. E. Machin, Wave propagation along flagella, J. Exp. Biol. **35**, 796 (1958).
[17] J. Lubliner and J. Blum, Model for bend propagation in flagella, J. Theor. Biol. **31**, 1 (1971).
[18] U. Goodenough and J. Heuser, Substructure of the outer dynein arm, J. Cell Biol. **95**, 798 (1982).
[19] B. Afzelius, R. Dallai, S. Lanzavecchia, and P. Bellon, Flagellar structure in normal human spermatozoa and in spermatozoa that lack dynein arms, Tissue Cell **27**, 241 (1995).
[20] D. M. Woolley, R. F. Crockett, W. D. I. Groom, and S. G. Revell, A study of synchronisation between the flagella of bull spermatozoa, with related observations, J. Exp. Biol. **212**, 2215 (2009).
[21] R. A. Cross, Molecular motors: Dynein's gearbox, Curr. Biol. **14**, R355 (2004).
[22] C. Lindemann and A. Hunt, Does axonemal dynein push, pull, or oscillate? Cell Motil. Cytoskel. **56**, 237 (2003).
[23] C. Shingyoji, H. Higuchi, M. Yoshimura, E. Katayama, and T. Yanagida, Dynein arms are oscillating force generators, Nature **393**, 711 (1998).
[24] H. Kojima, E. Muto, H. Higuchi, and T. Yanagida, Mechanics of single kinesin molecules measured by optical trapping nanometry, Biophys J. **73**, 2012 (1997).
[25] H. Sakakibara, H. Kojima, Y. Sakai, E. Katayama, and K. Oiwa, Inner-arm dynein c of Chlamydomonas flagella is a single-headed processive motor, Nature **400**, 586 (1999).
[26] H. Kojima, M. Kikumoto, H. Sakakibara, and K. Oiwa, Mechanical properties of a single-headed processive motor, inner-arm dynein subspecies-c of chlamydomonasstudied at the single molecule level, J. Biol. Phys. **28**, 335 (2002).
[27] E. Hirakawa, H. Higuchi, and Y. Y. Toyoshima, Processive movement of single 22s dynein molecules occurs only at low atp concentrations, Proc. Natl. Acad. Sci. USA **97**, 2533 (2000).
[28] Y. Q. Gao, A simple theoretical model explains dynein's response to load, Biophys J. **90**, 811 (2006).
[29] T. Hamasaki, M. E. Holwill, K. Barkalow, and P. Satir, Mechanochemical aspects of axonemal dynein activity studied by *in vitro* microtubule translocation, Biophys J. **69**, 2569 (1995).
[30] H. C. Taylor and M. E. J. Holwill, Axonemal dynein: A natural molecular motor, Nanotechnology **10**, 237 (1999).
[31] Q. Chen, D. Y. Li, and K. Oiwa, The coordination of protein motors and the kinetic behavior of microtubule a computational study, Biophys. Chem. **129**, 60 (2007).
[32] Y. Imafuku, Y. Y. Toyoshima, and K. Tawada, Length dependence of displacement fluctuations and velocity in microtubule sliding movement driven by sea urchin sperm outer arm β dynein in vitro, Biophys. Chem. **67**, 117 (1997).
[33] D. Lorch, C. Lindemann, and A. Hunt, The motor activity of mammalian axonemal dynein studied *in situ* on doublet microtubules, Cell Motil. Cytoskel. **65**, 487 (2008).
[34] R. Vale and Y. Toyoshima, Rotation and translocation of microtubules *in vitro* induced by dyneins from Tetrahymena cilia, Cell **52**, 459 (1988).
[35] X. Yang, R. Dillon, and L. Fauci, An integrative computational model of multiciliary beating, Bull. Math. Biol. **70**, 1192 (2008).
[36] C. J. Brokaw, Bend propagation by a sliding filament model for flagella, J. Exp. Biol. **55**, 289 (1971).
[37] C. J. Brokaw, Computer simulation of flagellar movement: I. Demonstration of stable bend propagation and bend initiation by the sliding filament model, Biophys. J. **12**, 564 (1972).
[38] C. J. Brokaw, Microtubule sliding in swimming sperm flagella: Direct and indirect measurements on sea urchin and tunicate spermatozoa, J. Cell Biol. **114**, 1201 (1991).
[39] C. J. Brokaw, Simulating the effects of fluid viscosity on the behavior of sperm flagella, Math. Methods Appl. Sci. **24**, 1351 (2001).
[40] R. H. Dillon, L. J. Fauci, and C. Omoto, Mathematical modeling of axoneme mechanics and fluid dynamics in ciliary and sperm motility, Dynam. Contin. Discrete Impuls. Syst.: Series A **10**, 745 (2003).
[41] R. H. Dillon, L. J. Fauci, and X. Yang, Sperm motility and multiciliary beating: An integrative mechanical model, Comput. Math. Appl. **52**, 749 (2006).
[42] C. B. Lindemann, A geometric clutch hypothesis to explain oscillations of the axoneme of cilia and flagella, J. Theor. Biol. **168**, 175 (1994).
[43] C. Lindemann, Geometric clutch model version 3: The role of the inner and outer arm dyneins in the ciliary beat, Cell Motil. Cytoskel. **52**, 242 (2002).
[44] R. Kamiya, Exploring the function of inner and outer dynein arms with chlamydomonas mutants, Cell Motil. Cytoskel. **32**, 98 (1995).

[45] R. Yamamoto, K. Song, H. Yanagisawa, L. Fox, T. Yagi, M. Wirschell, M. Hirono, R. Kamiya, D. Nicastro, and W. Sale, The mia complex is a conserved and novel dynein regulator essential for normal ciliary motility, J. Cell Biol. **201**, 263 (2013).

[46] S. Namdeo, S. N. Khaderi, and P. R. Onck, Numerical modelling of chirality-induced bi-directional swimming of artificial flagella, Proc. R. Soc. A **470**, 20130547 (2014).

[47] S. Namdeo, S. N. Khaderi, J. M. J. den Toonder, and P. R. Onck, Swimming direction reversal of flagella through ciliary motion of mastigonemes, Biomicrofluidics **5**, 034108 (2011).

[48] S. N. Khaderi, M. G. H. M. Baltussen, P. D. Anderson, D. Ioan, J. M. J. den Toonder, and P. R. Onck, Nature-inspired microfluidic propulsion using magnetic actuation, Phys. Rev. E **79**, 046304 (2009).

[49] S. Namdeo, S. N. Khaderi, and P. R. Onck, Swimming dynamics of bidirectional artificial flagella, Phys. Rev. E **88**, 043013 (2013).

[50] S. Ishijima and Y. Hiramoto, Flexural rigidity of echinoderm sperm flagella, Cell Struct. Funct. **19**, 349 (1994).

[51] F. Pampaloni, G. Lattanzi, A. Jonáš, T. Surrey, E. Frey, and E.-L. Florin, Thermal fluctuations of grafted microtubules provide evidence of a length-dependent persistence length, Proc. Natl. Acad. Sci. USA **103**, 10248 (2006).

[52] M. Kikumoto, M. Kurachi, V. Tosa, and H. Tashiro, Flexural rigidity of individual microtubules measured by a buckling force with optical traps, Biophys. J. **90**, 1687 (2006).

[53] H. Felgner, R. Frank, and M. Schliwa, Flexural rigidity of microtubules measured with the use of optical tweezers, J. Cell Sci. **109**, 509 (1996).

[54] F. Gittes, B. Mickey, J. Nettleton, and J. Howard, Flexural rigidity of microtubules and actin filaments measured from thermal fluctuations in shape, J. Cell Biol. **120**, 923 (1993).

[55] D. W. Pelle, C. J. Brokaw, K. A. Lesich, and C. B. Lindemann, Mechanical properties of the passive sea urchin sperm flagellum, Cell Motil. Cytoskel. **66**, 721 (2009).

[56] H. Gadêlha, E. A. Gaffney, and A. Goriely, The counterbend phenomenon in flagellar axonemes and cross-linked filament bundles, Proc. Natl. Acad. Sci. USA **110**, 12180 (2013).

[57] T. Guérin, J. Prost, and J.-F. Joanny, Dynamical behavior of molecular motor assemblies in the rigid and crossbridge models, Eur. Phys. J. E **34**, 1 (2011).

[58] D. Oriola, H. Gadêlha, C. Blanch-Mercader, and J. Casademunt, Subharmonic oscillations of collective molecular motors, Europhys. Lett. **107**, 18002 (2014).

[59] S. Ishijima, The velocity of microtubule sliding: Its stability and load dependency, Cell Motil. Cytoskel. **64**, 809 (2007).

[60] C. J. Brokaw, Molecular mechanism for oscillation in flagella and muscle, Proc. Natl. Acad. Sci. USA **72**, 3102 (1975).

[61] S. Gueron and K. Levit-Gurevich, Computation of the internal forces in cilia: Application to ciliary motion, the effects of viscosity, and cilia interactions, Biophys J. **74**, 1658 (1998).

[62] G. Taylor, Analysis of the swimming of microscopic organisms, Proc. R. Soc. London A **209**, 447 (1951).

[63] G. Taylor, The action of waving cylindrical tails in propelling microscopic organisms, Proc. R. Soc. London A **211**, 225 (1952).

[64] J. Gray and G. J. Hancock, The propulsion of sea-urchin spermatozoa, J. Exp. Biol. **32**, 802 (1955).

[65] S. K. Namdeo, Flagellar hydrodynamics of biological and biomimetic microswimmers, Ph.D. thesis, University of Groningen, Groningen, 2014.

[66] C. J. Brokaw, Effects of viscosity and ATP concentration on the movement of reactivated sea-urchin sperm flagella, J. Exp. Biol. **62**, 701 (1975).

[67] R. Annabattula, W. Huck, and P. Onck, Micron-scale channel formation by the release and bond-back of pre-stressed thin films: A finite element analysis, J. Mech. Phys. Solids **58**, 447 (2010).

[68] R. D. Cook, D. S. Malkus, M. E. Plesha, and R. J. Witt, *Concepts and Applications of Finite Element Analysis* (John Wiley & Sons, New York, 2002).

[69] C. Pozrikidis, *A Practical Guide to Boundary-Element Methods with the Software Library BEMLIB* (Chapman & Hall/CRC, Boca Raton, FL, 2002).

[70] S. N. Khaderi and P. R. Onck, Fluid-structure interaction of three-dimensional magnetic artificial cilia, J. Fluid Mech. **708**, 303 (2012).